A STRATEGY FOR TIME-TO-DEPTH CONVERSION AND VELOCITY ESTIMATION

L. S. S. Valente, H. B. Santos, J. C. Costa, and J. Schleicher

email: *hbuenos@gmail.com, js@ime.unicamp.br*

keywords: *Time-to-depth conversion, velocity model building, depth migration, image ray*

ABSTRACT

We present a strategy to time-to-depth conversion and velocity estimation based only on the image-wavefront propagation. It has two main features: (1) it computes the velocity field and the traveltime directly, avoiding the ray-tracing step; and (2) it requires only the knowledge of the image-wavefront at the previous time step. As a consequence, our method tends to be faster than usual techniques and does not carry the constraints and limitations inherent to common ray-tracing strategies. We have tested the feasibility of the method on a synthetic Gaussian velocity anomaly as well as on the original Marmousi velocity model and two smoothed versions of it. Moreover, we migrated the Marmousi data set using the estimated depth velocity models. Our results indicate that the present strategy can be used to construct starting models for velocity-model building in depth migration and/or tomographic methods.

INTRODUCTION

The need to investigate regions with complex geology has encouraged the development of imaging methods that act in the depth domain. Important examples are prestack depth migration (PSDM) and full-waveform tomography (FWT) techniques. However, the application of these methods faces at least two problems: they require (1) an accurate velocity macromodel and (2) large computation power.

In contrast, time migration has proved to be a very fast and robust process, making it routinely employed for seismic imaging. Moreover, time velocity-model building is a very well understood process, leading to high-quality migration velocity models in time. Therefore, it is highly desirable to construct starting models for depth techniques from these time-domain velocity models by means of time-to-depth conversion.

While vertical conversion from time to depth has been routinely employed for a long time, Hubral (1977) was the first to recognize the need of taking lateral displacements into account. He demonstrated that time- and depth-domain coordinates are interconnected by the so-called image ray. More recently, Cameron et al. (2007, 2008) derived the theoretical relation between the time-migration velocity and seismic velocity using image-ray theory and paraxial ray-tracing theory (Popov et al., 1978; Červeny, 2001; Popov, 2002). Their algorithm consists of image-ray tracing to convert time Dix velocities into ray coordinates velocities and then time-to-depth convert them based on Dijkstra-like fast marching methods (Sethian, 1999a,b). Iversen and Tygel (2008) proposed a similar but more efficient technique that even in 3D requires only a single-azimuth time-migration velocity field as an input to construct the depth velocity field.

Despite being a very attractive method, time-to-depth conversion is an ill-posed problem (Cameron et al., 2007). It aggregates the limitations of all involved steps, that is, the constraints involved in time migration, ray-tracing, and Dix-based velocity conversion (Iversen and Tygel, 2008). Thus, regularization is essential for adequate time-to-depth conversion. Such a regularization can be added in two phases of the process: (1) during the estimation of the Dix velocity field from an estimated time-migration velocity field, and (2) during the image-ray tracing. Valente et al. (2009) compared the three conversion techniques of Cameron et al. (2007), Cameron et al. (2008), and Iversen and Tygel (2008). They demonstrated that the

different procedures react differently to different kinds of regularization. However, although the image-ray trajectories and the resulting depth velocity models depended on the regularization employed, the corresponding final depth images were very similar.

The objective of the present work is to present an alternative algorithm for the time-to-depth conversion, which does not require image-ray tracing. Instead, it simulates the propagation of an image-wavefront in the subsurface. Our approach has the advantage of directly computing the velocity field and the traveltime. We test the approach on a synthetic Gaussian example and on the Marmousi data set. For the latter, we use Fourier Finite-difference (FFD) migration based on complex Padé approximations (Amazonas et al., 2007) to evaluate the quality of the depth-migrated images.

TIME-TO-DEPTH CONVERSION ALGORITHMS

We start with the formulation of the time-to-depth-conversion inverse problem based on image-ray theory and a brief description of some of the proposed newer algorithms.

Two-dimensional inverse problem

Consider an image point at coordinates (γ, τ) in a time migrated section, with $\gamma_{\text{min}} \leq \gamma \leq \gamma_{\text{max}}$ and $0 \leq \tau \geq \tau_{\text{max}}$. This image point can be associated with an image-ray that has reached the acquisition surface at the position γ in time τ. The problem of time-to-depth conversion consists of tracing this image-ray back into the medium together with a family of rays, associated with a plane wave that tangent to the acquisition surface at γ, until the time τ is consumed and the ray has reached its position $\mathbf{x} = (x, z)$ in the subsurface.

In other words, we want to simultaneously solve the set of equations for kinematic and dynamic ray tracing with plane-wave initial conditions. This set can be represented in two dimensions as

$$\begin{aligned} \frac{d\mathbf{x}}{d\tau} &= v^2(\mathbf{x})\mathbf{p}\,, \\ \frac{d\mathbf{p}}{d\tau} &= -\frac{1}{v(\mathbf{x})}\nabla_{\mathbf{x}} v(\mathbf{x})\,, \\ \frac{\partial Q}{\partial \tau} &= v^2(\mathbf{x})P\,, \\ \frac{\partial P}{\partial \tau} &= -\frac{1}{v(\mathbf{x})}\frac{\partial^2 v}{\partial \eta^2}\,Q\,, \end{aligned} \tag{1}$$

where η denotes the coordinate direction perpendicular to the ray. The initial conditions for image-ray tracing read

$$\mathbf{x}(\tau=0) = (\gamma, 0)\,, \quad \mathbf{p}(\tau=0) = \frac{\hat{\mathbf{z}}}{v^{\text{Dix}}(\mathbf{x}(\tau=0))}\,, \quad Q(\tau=0) = 1\,, \quad P(\tau=0) = 0 \tag{2}$$

where $\hat{\mathbf{z}}$ is the unit vector in the vertical direction.

Inversion algorithm

As an alternative to simplify the computation of the derivatives along the image-rays, Cameron et al. (2007) proposed an image-ray tracing algorithm which fits the image-wavefront by polynomial curves. Based on this algorithm, Valente (2013) proposed an additional regularization to the fitting, which increases the choice of the degree of the polynomial.

Only a little later, Cameron et al. (2008) presented a new ray tracing algorithm, in which the last two equations of system (2) are integrated based on the Lax-Friedrichs method (Lax, 1954), resulting in the scheme

$$\begin{aligned} P_j^{n+1} &= \frac{P_{j+1}^n + P_{j-1}^n}{2} - \frac{\Delta\tau}{4\Delta\gamma^2 v_j^n}\left(\frac{v_{j+2}^n - v_j^n}{Q_{j+1}^n} - \frac{v_j^n - v_{j-2}^n}{Q_{j-1}^n}\right)\,, \\ \frac{1}{Q_j^{n+1}} &= \frac{1}{Q_j^n} - \frac{\Delta\tau}{2}\left[(v_j^n)^2 P_j^n + (v_j^{n+1})^2 P_j^{n+1}\right]\,, \end{aligned} \tag{3}$$

where P_j^n denotes the value of P at the jth image-ray at γ_j and at the nth time sample τ_n. Moreover, in 2D v_j^n denotes the Dix velocity $v^{\text{Dix}}(\gamma_j, \tau_n)$ and in 3D, it denotes its square. In this method, no additional regularization is needed. The regularization is intrinsically performed by the P-averages that are computed along the wavefront of the image-wave, in this way avoiding instabilities in the FD scheme by damping high frequencies.

After the application of the any of the cited inversion algorithms, the results are the image-rays and/or image-wavefronts and, above all, the velocity field $v(\mathbf{x}(\gamma, \tau))$ in depth along the image rays trajectories. Therefore, this velocity field is given on a non-regular grid. One way to transfer this field onto a regular grid is direct interpolation at the regular grid points and extrapolation in the border regions. Cameron et al. (2007) describe a very efficient algorithm to solve this problem, using the eikonal equation based on the *fast-marching* method (Sethian, 1999a,b). This provides not only the depth velocity field $v(\mathbf{x})$, but also $\tau(\mathbf{x})$ and $\gamma(\mathbf{x})$ on a regular grid. The latter two fields can be used in the conversion of time-migrated images to depth-migrated images.

Cameron et al. (2007) also described another way to approach the problem by means of the level-set method (Sethian, 1999b).This method boils down to propagate the image-wavefront tangent to the acquisition surface in time $\tau = 0$ back into the subsurface. To do so, the image-wavefront is represented as a zero level of a two-dimensional function $\phi(\mathbf{x})$. Two two-dimensional functions $p(\mathbf{x})$ and $q(\mathbf{x})$ are also incorporated along the image-wavefront, defined in such a way that, for each time interval $\Delta\tau$ they are equivalent to the values of P and Q, respectively. These functions satisfy the equation system

$$\begin{aligned} \frac{\partial \phi}{\partial \tau} &= v(\mathbf{x}) \, \|\nabla \phi\| \\ \frac{\partial q(\mathbf{x})}{\partial \tau} &= v^2(\mathbf{x}) p(\mathbf{x}) \\ \frac{\partial p(\mathbf{x})}{\partial \tau} &= \frac{1}{v(\mathbf{x})} \frac{\partial^2 v}{\partial \eta^2} q(\mathbf{x}) \, , \end{aligned} \tag{4}$$

where the second derivative of v in the direction perpendicular to the ray can be represented as

$$\frac{\partial^2 v}{\partial \eta^2} = \left\| \frac{1}{\nabla \phi} \frac{\partial \phi}{\partial x} \right\|^2 \frac{\partial^2 v}{\partial x^2} - 2 \left(\frac{1}{\nabla \phi} \frac{\partial \phi}{\partial x} \cdot \frac{1}{\nabla \phi} \frac{\partial \phi}{\partial z} \right) \frac{\partial^2 v}{\partial x \partial z} + \left\| \frac{1}{\nabla \phi} \frac{\partial \phi}{\partial z} \right\|^2 \frac{\partial^2 v}{\partial z^2} \, . \tag{5}$$

From equation (2), we find the initial conditions for the auxiliary functions p and q as

$$q(\mathbf{x}(\tau = 0)) = 1 \, , \qquad p(\mathbf{x}(\tau = 0)) = 0 \, . \tag{6}$$

This scheme inherently uses the fast-marching conversion algorithm to calculate the velocity field $v(\mathbf{x})$.

Based on the algorithm of the level-set method, we propose an alternative strategy to perform the time-to-depth conversion. This new strategy has the advantage of directly obtaining the velocity field $v(\mathbf{x})$ and the traveltime $\tau(\mathbf{x})$, avoiding to calculate the auxiliary functions $p(\mathbf{x})$ and $q(\mathbf{x})$. By means of a modified fast-marching conversion algorithm, we can directly determine the matrix $\gamma(\mathbf{x})$ of image-ray emergence points from the already known values of $v(\mathbf{x})$ and $\tau(\mathbf{x})$. For details, see Valente (2013).

The wavefront-construction algorithm proposed in this work is slightly different from other algorithms discussed in previous works. For example, Vinje et al. (1993) construct the wavefront checking neighbouring rays for significant deviation or crossing, adding new rays in the first case and removing one of the crossing rays in the second one. The new rays start at the midpoint between two known rays with ray quantities obtained by linear interpolation. Furthermore, the authors also use linear interpolation to output the involved ray quantities on a regular grid. In a different strategy, Silva et al. (2009) use a finite-difference scheme to evolve the wavefront along the image ray. To determine the ray quantities at the new wavefront, this scheme makes use of the information at two points on the previous wavefront.

In this work, we proceed in yet another way. The principal advantage of our proposed algorithm is that the ray quantities are immediately interpolated at the horizontal coordinates of the given grid, determining the vertical coordinate of the wavefront accordingly. In this way, we avoid the need to add or remove points on the wavefront. Moreover, this procedure requires the final interpolation of the output quantities in the vertical direction only. For the propagation, it needs only the knowledge of the image-wavefront at the previous time step.

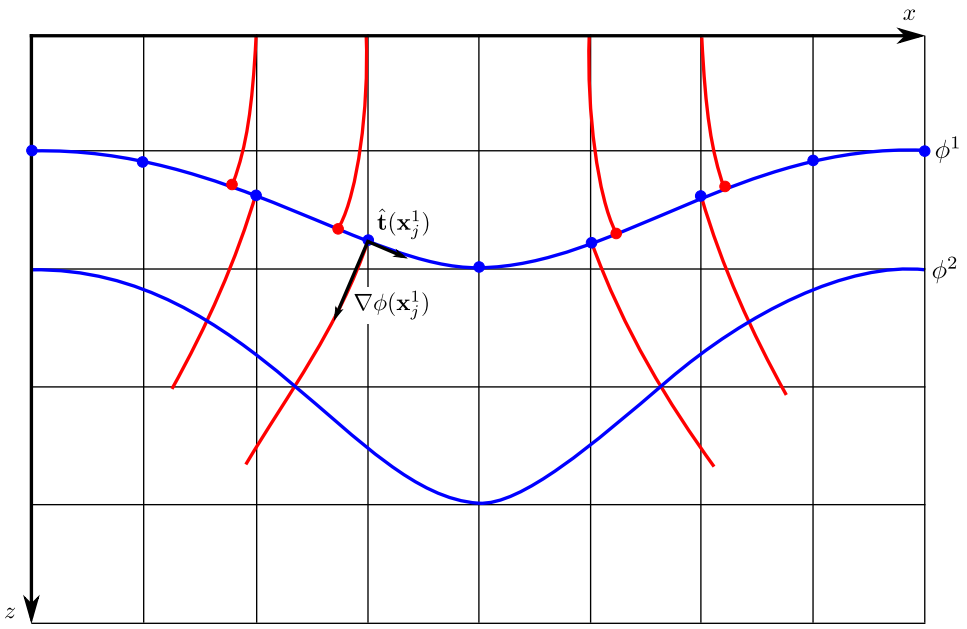

Figure 1: Sketch of the image-wavefront propagation algorithm. The ray quantities are not computed where the image-ray paths intersect the desired wavefront (red dots), but rather along vertical lines coincident with the lateral positions of the grid (blue dots). The next step starts from these new base points using tangent vector $\hat{\mathbf{t}}$ and the traveltime gradient $\nabla\phi$.

The first step of our algorithm is to propagate the image-wavefront $\phi(\mathbf{x})$ in the direction of its gradient $\nabla\phi$, integrating the system

$$\begin{aligned} x_j^{n+1/2} &= x_j^n + v_j^n \, (\mathbf{n}\cdot\hat{\mathbf{x}})_j^n \, \Delta\tau \,, \\ z_j^{n+1/2} &= z_j^n + v_j^n \, (\mathbf{n}\cdot\hat{\mathbf{z}})_j^n \, \Delta\tau \end{aligned} \tag{7}$$

to obtain the coordinates (red points in Figure 1) of the image rays on new wavefront $\phi^{n+1}(\mathbf{x}(\gamma))$ from the those of the previous one, $\phi^n(\mathbf{x}(\gamma))$, where j indicates the number of the image ray and n indicates the time step, as before. The direction $\mathbf{n} = \nabla\phi / \|\nabla\phi\|$ of the gradient at each point along the wavefront is obtained by rotating by -90° the unit tangent vector to the wavefront, approximated by

$$\hat{\mathbf{t}} = \frac{(x_{j+1} - x_j, z_{j+1} - z_j)}{\sqrt{(x_{j+1} - x_j)^2 + (z_{j+1} - z_j)^2}} \,. \tag{8}$$

From the set of points $\mathbf{x}^{n+1/2}$, we can find the points on the wavefront $\mathbf{x}^n$ that intersect the vertical grid lines (blue points in Figure 1). They are given by $x^{n+1} = \gamma$ and $z^{n+1} = z(x^{n+1}, \tau^{n+1})$, where the vertical coordinate is determined by means of linear interpolation. In other words, we redefine the calculation points so that they fall exactly on the lateral positions where the wavefront intersects the grid (see Figure 1). In this way, the sampling along the wavefront remains always regular, avoiding the need to add or remove rays.

At the next time step, the algorithm starts at the image-wavefront at these new coordinates (Figure 1) and the velocity field is determined from

$$v(\mathbf{x}) \equiv v^{\text{Dix}}(\gamma = x, \tau(\mathbf{x})) \,. \tag{9}$$

We refer to this wavefront-construction strategy as wavefront propagation, because it does not follow any single image-rays through the model.

NUMERICAL EXAMPLES

We tested our new wavefront-propagation strategy by applying it to different synthetic data sets. We start with a very simple smooth Gaussian model. Next, we applied it to data from different versions of the Marmousi model. In all cases, we compare the determined depth velocity model to those estimated by other time-to-depth conversion methods. Finally, we complement our numerical evaluation with a comparison of the depth-migrated sections obtained using the complex Padé Fourier finite-difference technique of Amazonas et al. (2007).

Gaussian model

As a first test, we applied time-to-depth conversion using our new wavefront-construction strategy to the same smooth Gaussian velocity model used in Cameron et al. (2007). The velocity distribution in this model (see Figure 2(a)) is given by

$$v(x,z) = 2 + 2\exp\{-(x^2 + (z-2)^2)\}\,, \tag{10}$$

where $x \in$ [-3, 3] and $z \in$ [0, 2].

As the input to the conversion, we computed the Dix velocity depicted in Figure 2(b) with a time sampling of 4 ms (two-way travel time). We start by mapping it from time to depth using image-ray tracing and *fast marching* conversion as proposed by Cameron et al. (2008). The result is presented in Figure 2(c). We then converted the same time velocity model using the image-wavefront propagation strategy proposed here. The result can be seen in Figure 2(d). There are notable differences between the converted depth models in Figures 2(c) and 2(d). These differences are highlighted in Figures 2(e) and 2(f), which show the relative error of the converted models as compared to the true one (Figure 2(a)). We observe that the errors of both methods are relatively small in the shallow part, above 1 km depth. However, while the image-ray procedure then accumulates larger errors the wavefront-propagation technique remains fairly accurate. Figure 2(e) shows that the extracted velocity using image-ray tracing gets worse as the depth increases, reaching error values around 12%. This happens because the curvature of the rays increase with depth. On the other hand, the maximum relative error of the image-wavefront propagation (Figure 2(f)) is about 0.6%, indicating that our method is quite accurate even being a first-order approximation.

Figures 2(g) and 2(h) represent an alternative way to evaluate the quality of the two procedures. They show the wavefronts as constructed by the two techniques for the models of Figures 2(c) and 2(d) in blue, over the corresponding wavefronts for the true model (Figure 2(a)) in back. The number at each line corresponds to the traveltime of the current wavefront. Again, we can see that both methods are quite similar in the shallow part, but the image-wavefront propagation provided better results for larger depths.

Marmousi model

Since our wavefront-propagation strategy does not require smooth input velocities, we could test it on the Marmousi velocity model (Versteeg, 1994), representing a more realistic geological setting. For a comparison to the conventional conversion procedures, we applied them to two differently smoothed versions.

Original Marmousi model without smoothing Paraxial ray theory needs a smooth velocity field without strong velocity variations. Otherwise, the ray field becomes irregular and cannot be trusted. As a consequence the time-to-depth conversion methods based on paraxial ray tracing can be applied only if the input model is smooth. In contrast, our new wavefront-propagation strategy can be applied to the original Marmousi model without smoothing. The reason is it is an adaptation of the level-set method (Cameron et al., 2007, 2008) that does not rely on the ray-tracing step. Therefore, we are able to evaluate its behaviour in a very complex situation. This example highlights an important feature of our method: It *does not require* any previous regularization. Thus, it can be applied directly in high-frequency models and/or noise corrupted models provided, for example, by automatic methods of velocity-model building.

Figure 3(a) shows the original Marmousi velocity model in depth without smoothing. As before, we compute the Dix velocity (Figure 3(b)) and use it as the input for the time-to-depth conversion by image-wavefront propagation. The resulting converted depth model is depicted in Figure 3(c).

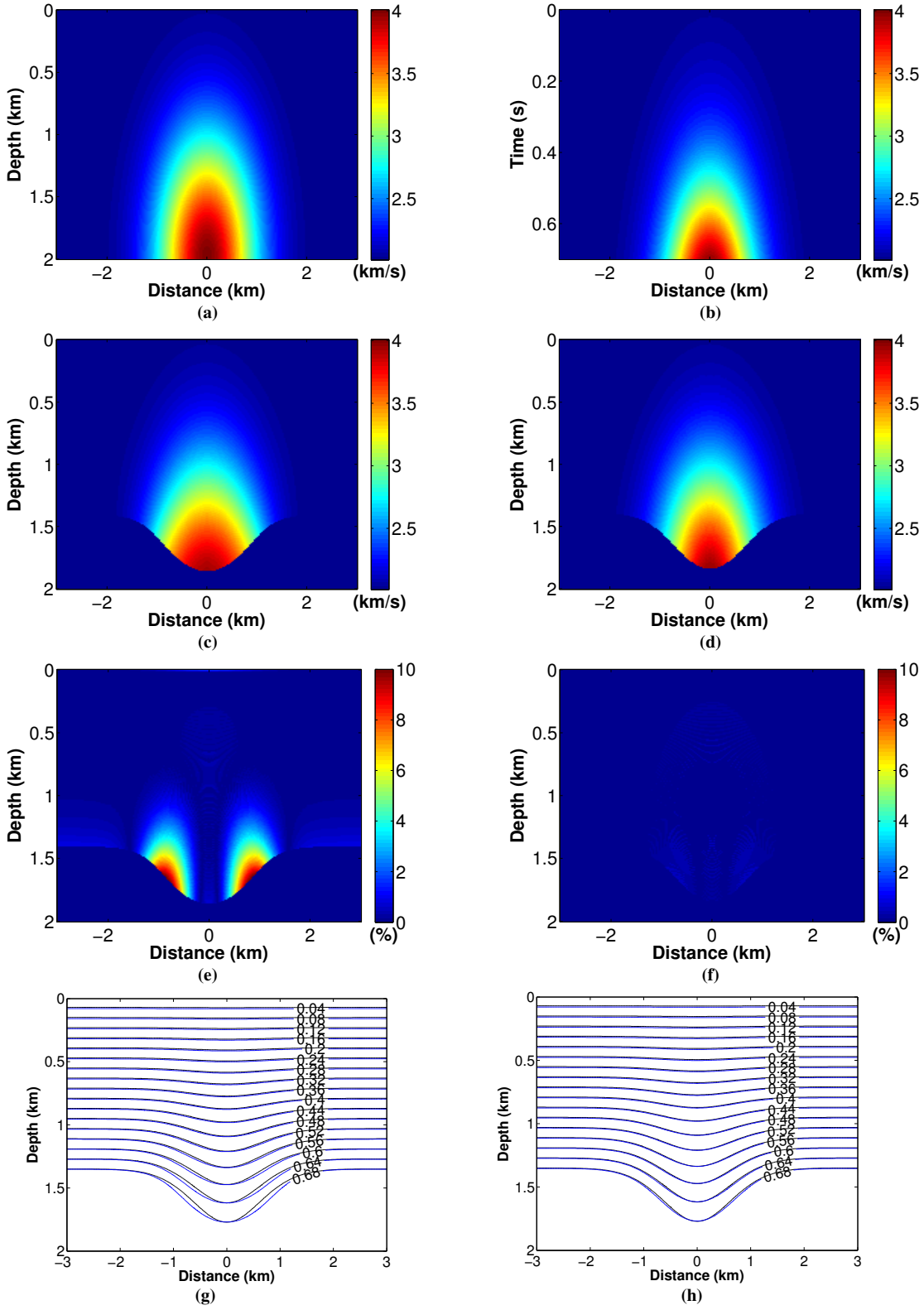

Figure 2: Synthetic test of time-do-depth conversion for a Gaussian-anomaly velocity model. True interval velocity model in (a) depth and (b) time. Time-to-depth conversion by (c) image-ray tracing and (d) image-wavefront propagation. Relative error of (f) image-ray tracing and (e) image-wavefront propagation. Wavefronts from (g) image-ray tracing (blue lines) and (h) image-wavefront propagation (blue lines), compared to wavefronts in the true model (black lines). Numbers indicate traveltimes in seconds.

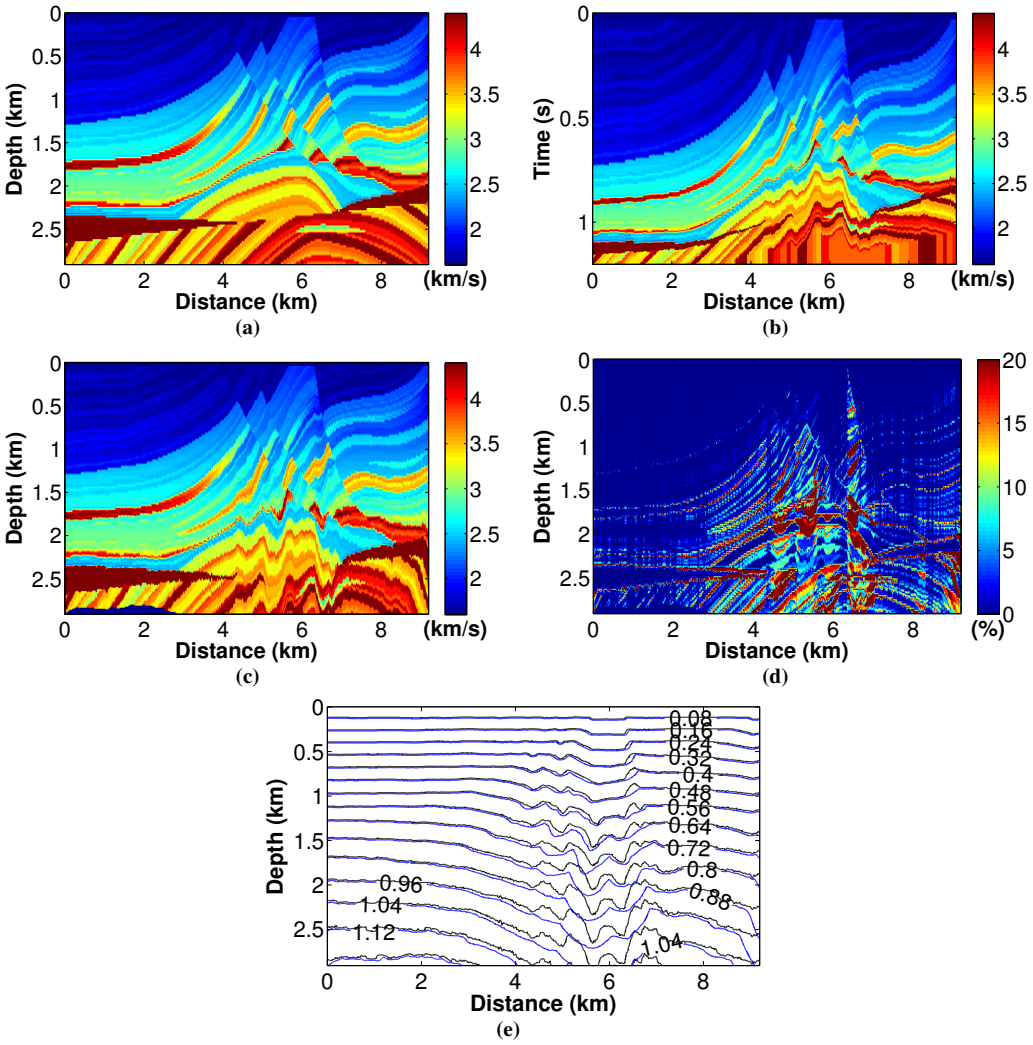

Figure 3: Test on the stratigraphic Marmousi velocity model without smoothing. (a) True Marmousi depth model. (b) Time interval velocity. (c) Time-to-depth conversion by image-wavefront propagation. (d) Relative model error. (e) Wavefronts in converted (blue lines) and true (black lines) models. Numbers indicate traveltimes in seconds.

We observe that time-to-depth conversion by image-wavefront propagation recovers a high-quality version of the original model in the central part down to a depth of about 1.5 km and in the sedimentary parts on the sides of the model down to the salt intrusions. Even the intrusions themselves and sediments below them are quite reasonably recovered. The high velocity of these salts do not seem to have a strong influence on the sediments below them.

The faults present in the central part of the Marmousi model bring out another interesting feature. Apparently, our technique does not suffer with the strong dip variation present in that area. However, below the strong lateral velocity variations in the central part of the model, where the time velocity model shows some high-frequency irregularities, these are amplified in the converted depth model.

The quality of the converted model is confirmed in Figure 3(d), which shows the relative error between the extracted velocity model (Figure 3(c)) and the true one (Figure 3(a)). The error accumulates in the regions of strong lateral velocity variations, where the image-ray principle is known to become problematic. Particularly at misplaced velocity contrasts, the error can locally reach almost 100%.

Finally, Figure 3(e) presents the superposition of the wavefronts. This figure confirms the previous observations, showing a better fit of the wavefronts in the upper and lateral parts of the model. Moreover,

we see in Figure 3(e) that even in the central parts of the model, the long wavelengths of the wavefronts in the extracted model adjust to those of the wavefronts in the true model.

Smoothed versions of the Marmousi model To allow for a comparison between the ray-tracing-based time-to-depth conversion techniques of Cameron et al. (2007, 2008) with our image-wavefront propagation, we need a smooth input velocity model. For this reason, we smoothed the original Marmousi velocity model (Figure 3(a)) by a single pass of a moving-average filter. In the first test, we used a 600 m$\times$600 m (50 by 50 points) window (see Figure 4(a)).

Figures 4(c) and 4(d) show the depth velocity models obtained, respectively, by image-ray and wavefront-propagation conversion of the Dix velocities in Figure 4(b), and Figures 4(e) and 4(f) show their respective errors. As a first observation, we notice that both models resemble the original model quite closely. The errors of the conversion of the smooth model are much smaller than the ones from the conversion of the hard model (compare Figure 4(f) to Figure 3(d)). We conclude that, though not a requirement, conversion of a smooth model is advantageous for the wavefront-propagation method. As in the case of the Gaussian velocity anomaly, image-ray conversion produces, below a certain depth, significantly larger errors (up to 20%) than wavefront-propagation conversion (up to 7%), even in the sedimentary part of the model. In the image-ray converted model (Figure 4(c)), there are two near-vertical lines at distances of about 5 km and 7 km, where the converted velocities change rather abrupt. These are due to crossing image rays. This effect is not observable in the wavefront-propagation converted model (Figure 4(d)). The better quality of the latter model is also reflected in the better match of the wavefronts in Figure 4(h) than in the corresponding image-ray Figure 4(g).

The second test, where we used a 1200 m$\times$1200 m (100 by 100 points) window for the moving-average filter (see Figure 5(a)), confirms these findings. For this even smoother model, the converted models (Figures 5(c) and 5(d)) are even closer to the true model and the errors of both methods (Figures 5(e) and 5(f)) are smaller than in the previous case (up to 9% for image-ray conversion, 1.2% for wavefront-propagation conversion). The result of wavefront-propagation conversion (Figure 5(d)) is still superior to the one of image-ray conversion (Figure 5(c)), which is clearly visible in the error plots (Figures 5(e) and 5(f)) and also reflected in the better match of the wavefronts (Figures 5(g) and 5(h)). Though weaker, the abrupt velocity changes due to image-ray crossing are still visible in Figure 5(c).

MIGRATION RESULTS

We have shown that time-to-depth converted velocity models depend on the technique employed for the conversion. Moreover, it is known that depth migration is more susceptible to velocity variations than time migration. Thus, an important means to evaluate the achieved depth velocity models is by means of depth migrations. We used a two-dimensional Fourier finite-difference (FFD) migration with the complex Padé approximation as discussed in Amazonas et al. (2007). One of the reasons that led us to choose this method is that it was proven to be fast and robust. Another important point is that Amazonas et al. (2007) performed several depth migrations with different migration methods for the Marmousi data set and velocity model we use here. The use of their migration method allows us to compare our results to their migrated images, in this way increasing our information database.

For better comparison, all models presented in the last section were used to depth migrate the Marmousi data set with the same setup of Amazonas et al. (2007). We used a branch-cut rotation angle of $\alpha = 45^\circ$, a depth extrapolation step size of 6 m, and the source wavefield was computed using a Ricker wavelet with a 25-Hz peak frequency. Figures 6, 7 and 8 show the migrated images obtained with the models presented in Figures 3, 4 and 5 respectively.

Figure 6 compares the migration of the Marmousi dataset with the true Marmousi model (Figure 6(a)) to the one using the wavefront-propagation converted unsmoothed model (Figure 6(b)). While we recognize some deterioration of the image in Figure 6(b), particular in the lowermost part, the overall result is quite acceptable, indicating that the time-to-depth conversion has worked as expected.

The migrated image using the true smoothed model of the first example is already of a poorer quality (Figure 7(a)) than both images of Figure 6. The images obtained from the converted models (Figures 7(b) and 7(c)) are quite similar to Figure 7(a). As expected from the velocity models, the image obtained with the wavefront-propagation model (Figure 7(c)) is a little closer to the one from the true smooth model, with

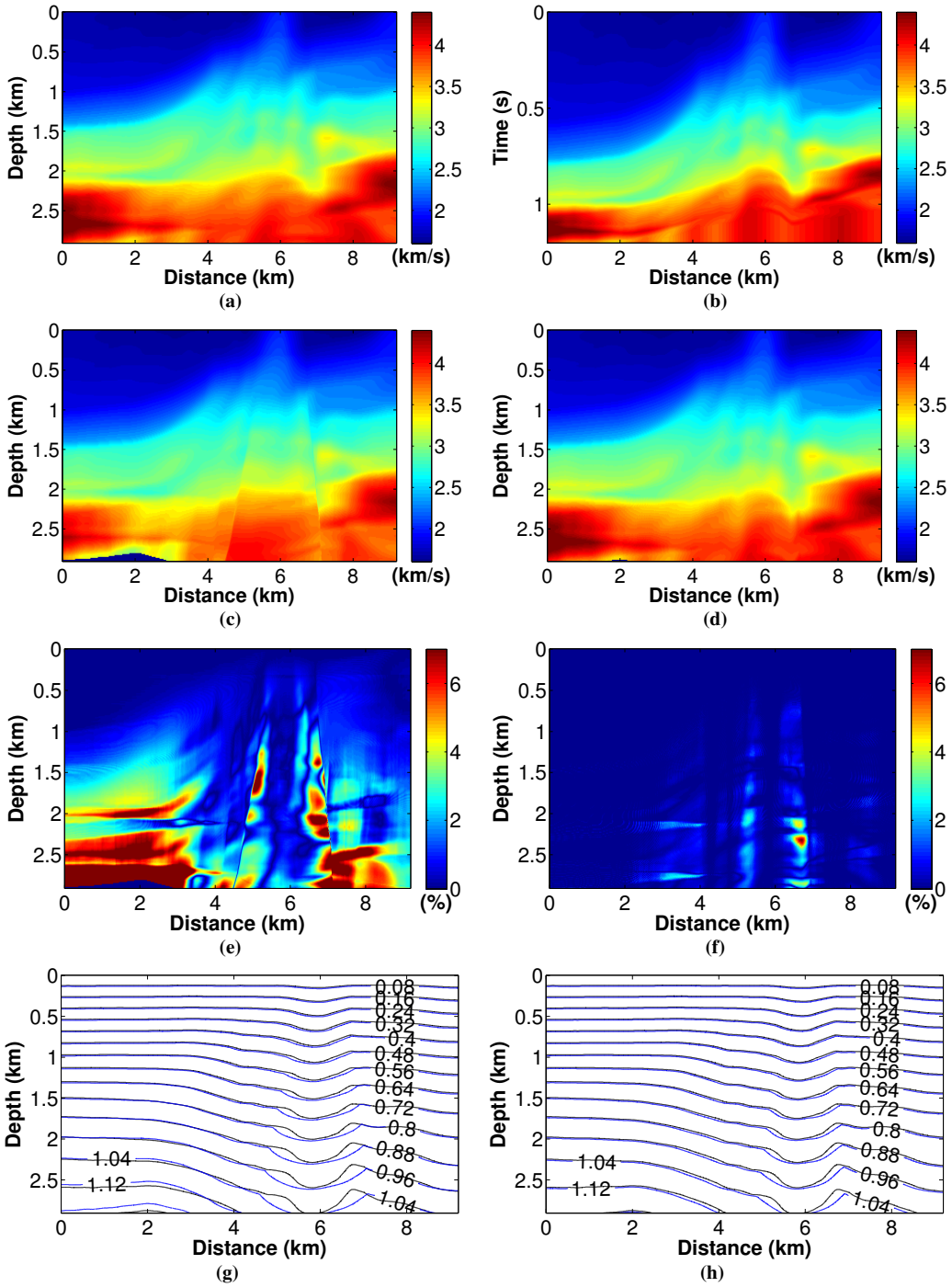

Figure 4: Test on a smoothed version of the Marmousi model of Figure 3(a). One pass of a moving average with a 600 m×600 m (50 by 50 points) window. (a) True depth model. (b) Time interval velocity. Time-to-depth conversion by (c) image ray-tracing and and (d) image-wavefront propagation. (e) Relative error of (c). (f) Relative error of (d). (g) Wavefronts (blue lines) in (c) and (h) wavefronts (blue lines) in (d), as compared to the wavefronts in the true model (black lines). Numbers indicate traveltimes in seconds.

the deviations in the image-ray image (Figure 7(b)) being located at and below the regions where the model errors are the largest (see Figure 4(e)).

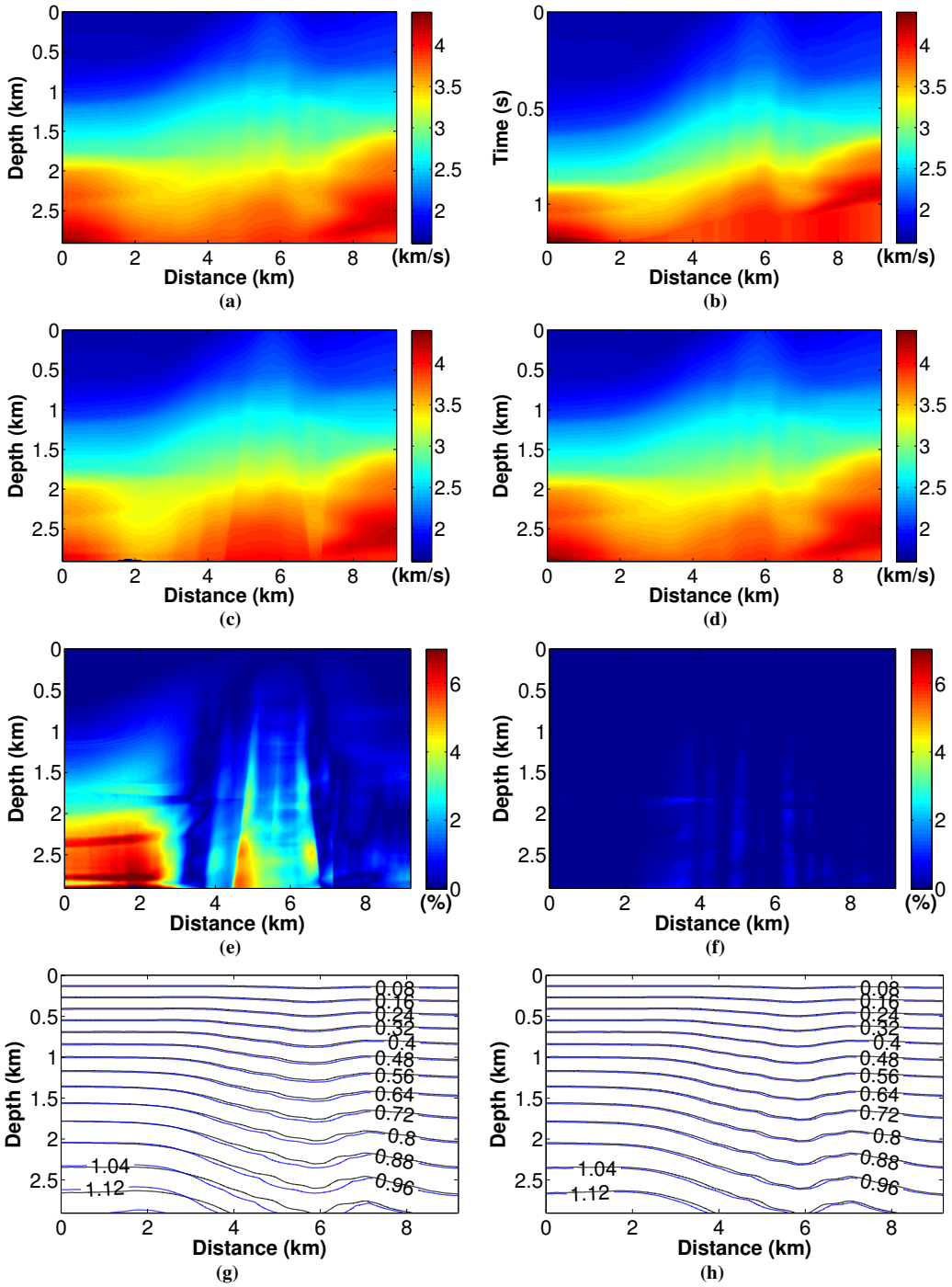

Figure 5: Test on a smoothed version of the Marmousi model of Figure 3(a). One pass of a moving average with a 1200 m×1200 m (100 by 100 points) window. (a) True depth model. (b) Time interval velocity. Time-to-depth conversion by (c) image ray-tracing and and (d) image-wavefront propagation. (e) Relative error of (c). (f) Relative error of (d). (g) Wavefronts (blue lines) in (c) and (h) wavefronts (blue lines) in (d), as compared to the wavefronts in the true model (black lines). Numbers indicate traveltimes in seconds.

The images in Figure 8 are even more similar to each other. Closer inspection reveals that again, the strongest deviations from the migration with the true model (Figure 8(a)) occur in the image-ray image

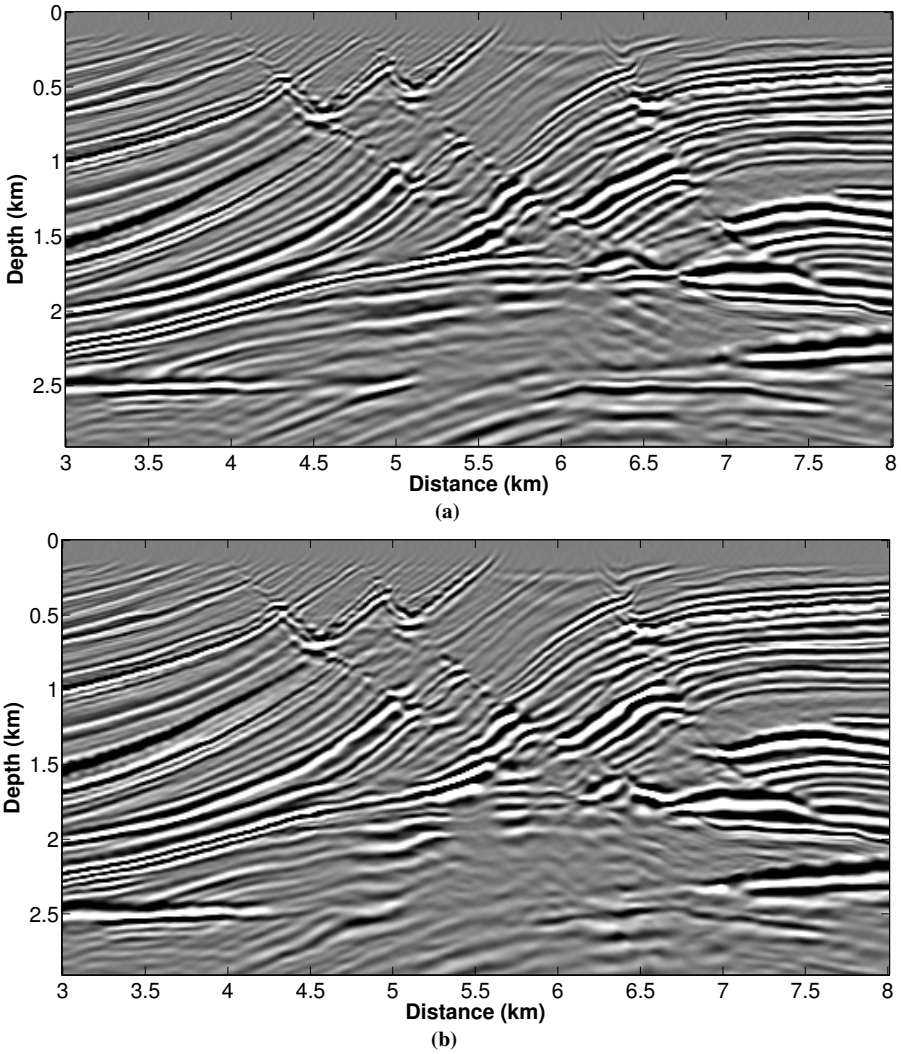

Figure 6: Prestack depth migrated sections of Marmousi data set using the velocity models of Figure 3(a) and (c) respectively.

(Figure 8(b)) at those parts where the model errors are the largest, while the wavefront-propagation image (Figure 8(c)) is now virtually indistinguishable from Figure 8(a).

CONCLUSION

We have presented a new strategy to perform wavefront-construction in image-ray-based time-to-depth conversion of velocity models. We make use of geometric considerations on a rectangular grid to move the base points to vertical lines instead of following individual image rays. In this way, we are able to reduce the computation time without any loss in accuracy. Our method allows to calculate the velocity and traveltime fields directly, avoiding the computation of certain parameters common in the ray-tracing methods. To proceed, the procedure requires only the knowledge of the image-wavefront of the previous time step.

We have tested our new procedure on a simple Gaussian velocity anomaly and in a more complex settings using smoothed and unsmoothed versions of the Marmousi model. We have found that our time-to-depth conversion provides satisfactory depth models. Since it does not rely on paraxial ray tracing, it even works in the presence of sharp velocity contrasts. In the smoothed models, it was able to provide remarkably accurate results down to greater depths than conventional methods that trace individual image

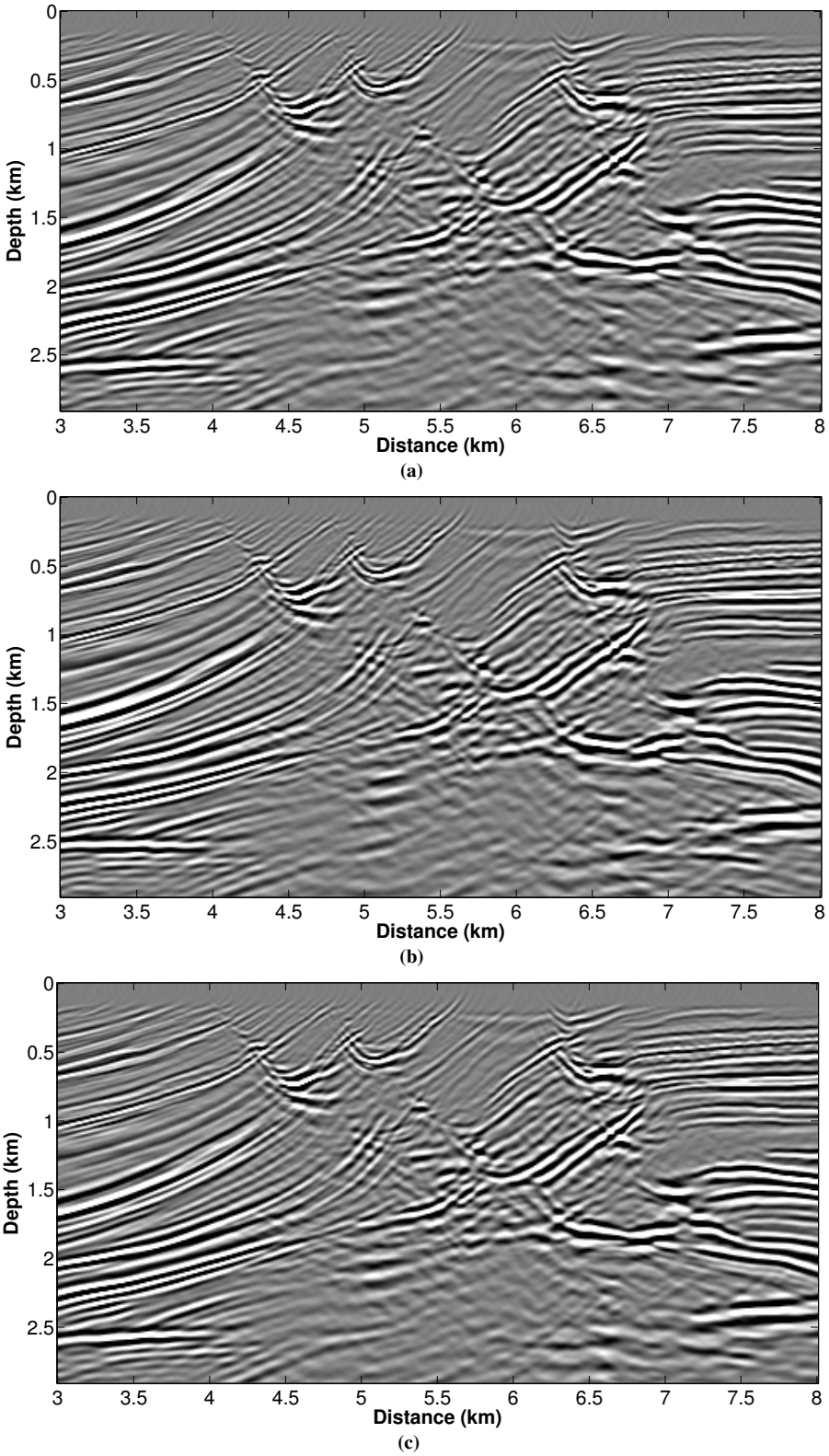

Figure 7: Prestack depth migrated sections of Marmousi data set using the velocity models of Figure 4(a), (c) and (d) respectively.

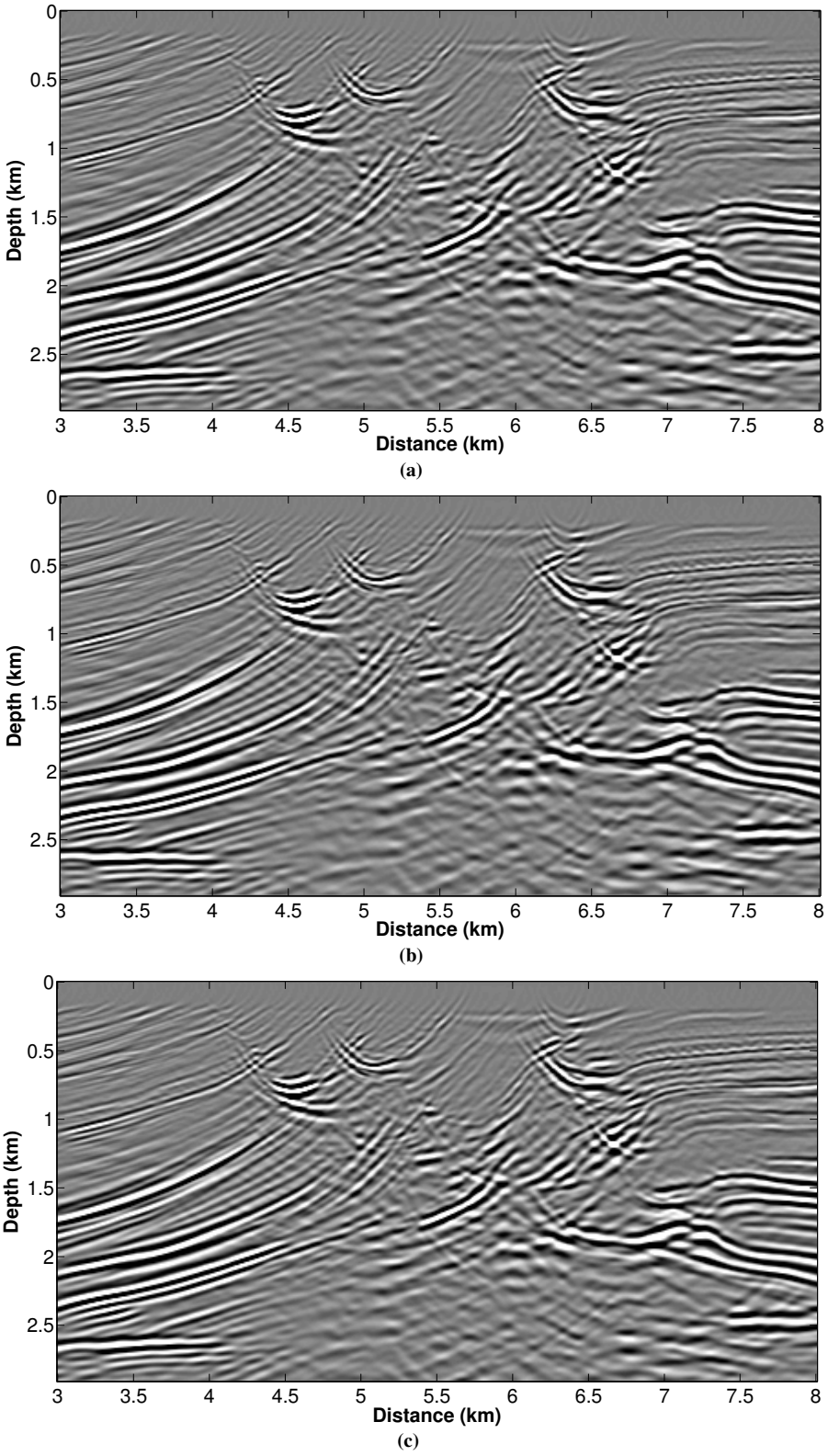

Figure 8: Prestack depth migrated sections of Marmousi data set using the velocity models of Figure 5(a), (c) and (d) respectively.

rays.

Results of depth migration of the synthetic Marmousi data using the depth-converted models indicate that these models preserve the quality of the time-domain models used as their input. Future work will assess the applicability of the method as a linker step in order to connect time velocity models computed by automatic migration velocity analysis techniques (see, e.g., Schleicher and Costa, 2009), with more sophisticated tomographic or migration-velocity-analysis methods in depth.

ACKNOWLEDGEMENTS

We acknowledge CAPES, CNPq, FINEP, PETROBRAS, ANP and CGG for financial support. The second author (HBS) thanks CGG-Brazil for his fellowship. Additional support for the authors was provided by the sponsors of the *Wave Inversion Technology (WIT) Consortium*.

REFERENCES

Amazonas, D., Costa, J. C., Schleicher, J., and Pestana, R. (2007). Wide-angle FD and FFD migration using complex padé approximations. *Geophysics*, 72(6):S215–S220.

Cameron, M. K., Fomel, and Sethian, J. A. (2008). Time-to-depth conversion and eismic velocity estimation using time-migration velocity. *Geophysics*, 73(5):VE205–VE210.

Cameron, M. K., Fomel, S. B., and Sethian, J. A. (2007). Seismic velocity estimation from time migration. *Inversion Problems*, 23:1329–1369.

Červeny, V. (2001). *Seismic ray theory*. Cambridge University Press, Cambridge.

Hubral, P. (1977). Time migration - some ray theoretical aspects. *Geophys Prospect*, 25(4):738–745.

Iversen, E. and Tygel, M. (2008). Image-ray tracing for joint 3D seismic velocity estimation and time-to-depth conversion. *Geophysics*, 73(3):S99–S114.

Lax, P. D. (1954). Weak solutions of hyperbolic equations and their numerical computation. *Communications in Pure and Applied Mathemetics*, 7:159–193.

Popov, M. M. (2002). *Ray Theory and Gaussian Beam Method for Geophysicists*. Editora da Universidade Federal da Bahia.

Popov, M. M., Pšenčík, I., and Červený, V. (1978). Computation of ray amplitudes in inhomogeneous media with curved interfaces. *Studia Geophysica et Geodaetica*, 22(3):248–258.

Schleicher, J. and Costa, J. C. (2009). Migration velocity analysis by double path-integral migration. *Geophysics*, 74(6):WCA225–WCA231.

Sethian, J. A. (1999a). Fast marching methods. *SIAM Review*, 41(2):199–235.

Sethian, J. A. (1999b). *Level set methods and fast marching methods*. Cambridge University Press, Cambridge.

Silva, E. F. F., Portugal, R., and Vicentini, A. (2009). Model rays for depth-to-time conversion. In *11th International Congress of the Brazilian Geophysical Society & EXPOGEF 2009, Salvador, Bahia, Brazil, 24-28 August 2009*. Society of Exploration Geophysicists and Brazilian Geophysical Society.

Valente, L. S. S. (2013). Evaluation of algorithms for the conversion of velocity models from time to depth. Master's thesis, Federal University of Pará. In Portuguese.

Valente, L. S. S., Costa, J. C., and Schleicher, J. (2009). Evaluation of time to depth conversion algorithms for depth velocity model building. *Annual WIT report*, 13:131–142.

Versteeg, R. (1994). The marmousi experience: Velocity model determination on a synthetic complex data set. *The Leading Edge*, 13(9):927–936.

Vinje, V., Iversen, E., and Gjøystdal, H. (1993). Traveltime and amplitude estimation using wavefront construction. *Geophysics*, 58(8):1157–1166.